Journal Name

COMMUNICATION

Optoelectronic properties of atomically thin ReSSe with weak interlayer coupling

Received 00th January 20xx,
Accepted 00th January 20xx

DOI: 10.1039/x0xx00000x

www.rsc.org/

Fucai Liu,[a,†] Shoujun Zheng,[b,†] Apoorva Chaturvedi,[a] Viktor Zólyomi,[c] Jiadong Zhou,[a] Qundong Fu,[a] Chao Zhu,[a] Peng Yu,[a] Qingsheng Zeng,[a] Neil D. Drummond,[d] Hong Jin Fan,[b] Christian Kloc,[a] Vladimir I. Fal'ko,[c] Xuexia He*,[a] Zheng Liu*[a,e]

Rhenium dichalcogenides, such as ReS_2 and $ReSe_2$, have attracted a lot of interests due to the weak interlayered coupling in these materials. Studies of rhenium based dichalcogenide alloys will help us understand the differences between each binary rhenium dichalcogenides. They will also extend the applications of two-dimensional (2D) materials through alloying. In this work, we studied the optoelectronic properties of ReSSe with S and Se ratio of 1:1. The band gap of ReSSe alloy is investigated by optical absorption spectra as well as theoretical calculations. The alloy shows weak interlayered coupling, as evidenced by the Raman spectrum. A field-effect transistor based on ReSSe shows typical n-type behavior with a mobility of about 3 $cm^2V^{-1}s^{-1}$ and an on/off ratio of 10^5, together with the in-plane anisotropic conductivity. The device also shows good photoresponse properties, with a photoresponsivity of 8 A/W. The results demonstrated here will provide new avenues for the study of 2D materials with weak interlayer interactions and in-plane anisotropy.

Owing to their interesting physical properties and promising applications in nanoelectronics, optoelectronics, and valleytronics[1-10], two-dimensional (2D) materials have attracted a lot of interests since the discovery of graphene. Graphene, a single layer of carbon atoms arranged in a honeycomb lattice, has shown extremely high mobilities[11, 12], a high Young's modulus[13], and an excellent thermal conductivity[14]. However, the absence of a band gap in graphene reduces its applicability in semiconducting and optoelectronic devices. This has triggered research interests in other semiconducting 2D materials. Among the 2D semiconductors that have been studied, transition-metal dichalcogenides (TMDs) are some of the most promising candidates for optoelectronic applications due to their direct band gaps and strong absorption[15-19]. The recently discovered black phosphorus (BP) has a direct band gap, increasing monotonically from ~0.3 eV in bulk to ~1.7 eV in a monolayer[20, 21]. It also shows high mobilities of up to 1000 $cm^2V^{-1}s^{-1}$ at room temperature[22, 23]. These properties make it suitable for applications such as broadband photodetectors, solar cells, and digital electronics[24, 25]. In addition, the bulk structure in BP opens up a new field for studying the in-plane anisotropy of 2D materials and designing conceptually new optoelectronic devices[26-28]. However, the poor environmental stability of BP restricts its applicability[29]. Discovering new, air-stable 2D materials with in-plane anisotropy and other novel functionality would be very rewarding.

Re dichalcogenides are promising candidates for the study of anisotropy. ReS_2 forms a distorted 1T structure with triclinic symmetry (Figure 1a)[30]. The Peierls distortion of the 1T structure results in buckled S layers and zigzag Re chains along one of the lattice vectors (*b*-axis) in the plane. As a consequence, the optical and electric properties in the layer plane are strongly anisotropic[31]. Exploiting the anisotropy of the electronic conductivity of ReS_2, an integrated inverter based on ReS_2 has been demonstrated[32]. Moreover, the interlayered coupling in ReS_2 is much weaker than other TMDs, with the adjacent monolayers being largely decoupled. Unlike other TMDs, from bulk to monolayers, the Raman spectrum shows almost no dependence on the thickness of ReS_2[33].

The unique properties of ReS_2 make Re compounds attractive for applications in novel optoelectronic devices. To realize high-efficiency solar cells or other optoelectronic devices based on Re compounds, it is crucially important to develop a strategy to tune their optical band gap. Band-gap engineering of TMDs has become urgent. Strain engineering and stacking of various 2D materials have been proposed as

[a]*School of Materials Science and Engineering, Nanyang Technological University, Singapore 639798, Singapore.*
[b]*Centre for Disruptive Photonic Technologies, School of Physics and Mathematics Sciences, Nanyang Technological University, Singapore 637371, Singapore.*
[c]*National Graphene Institute, University of Manchester, Booth St E, Manchester M13 9PL, United Kingdom*
[d]*Physics Department, Lancaster University, Lancaster LA1 4YB, United Kingdom.*
[e]*NOVITAS, Nanoelectronics Centre of Excellence, School of Electrical and Electronic Engineering, Nanyang Technological University, Singapore 639798.*
[†]*Authors contributed equally to this work*
**Address correspondence to z.liu@ntu.edu.sg (Z.L.), xxhe@ntu.edu.sg (X.H.)*

possible approaches to modify their band gaps[34-37]. In addition, alloying semiconductors with different band gaps has been widely adopted in the band-gap engineering of bulk semiconductors, as well as Mo- or W-based 2D materials[38-40]. By alloying 2D materials, not only the band gap, but also properties such as spin-orbit coupling can be engineered[41]. In this work, we have synthesized ReSSe alloys and exfoliated monolayer and few-layer ReSSe flakes, and studied their optical and electric properties. Few-layer ReSSe alloys show weak interlayered interactions, similar to ReS_2 layers. A device based on few-layer ReSSe shows a mobility of 3 $cm^2V^{-1}s^{-1}$ and an on/off ratio of 10^5. It also shows in-plane anisotropic conductivity. Good photoresponse, with a responsivity of around 8 A/W, is also observed. ReSSe alloys provide new candidates for the study of weak interlayer coupling and the design of new devices based on in-plane anisotropy.

Before exfoliation the ReSSe alloy, we first measured the absorption spectrum of ReSSe alloy as well as the parent compound ReS_2 and $ReSe_2$. Figure 1b shows the absorption spectra of ReS_2, ReSSe and $ReSe_2$, respectively. The exciton peaks are all clearly observed in these three compounds, indicating stable exciton state at room temperature due to the large exciton binding energy. The exciton peak (1.39 eV) is between the exciton peaks of ReS_2 (1.51 eV) and $ReSe_2$ (1.32 eV), indicating the effective band engineering of the alloy compounds. Atomically thin ReSSe flakes are prepared by the standard micromechanical exfoliation method. First, ReSSe single crystal was grown by the chemical vapour transport (CVT) method. Then the bulk crystals were exfoliated using Scotch tape and transferred onto Si substrates covered with 285 nm SiO_2. Flakes of different thicknesses were identified under a microscope. Figure 1c shows a typical optical image of ReSSe flakes, with thicknesses ranging from monolayer to four layers. Atomic force microscopy (AFM) was used to determine their exact thickness. As shown in Figure 1d and e, monolayer ReSSe is identified, the step height corresponds to the thickness of one ReSSe layer.

Raman spectroscopy is a powerful tool for studying phonons in 2D materials. Figure 2a shows the Raman spectra of ReSSe flakes, with the thickness ranging from monolayer to five layers, and bulk ReSSe. More than ten peaks were observed in the range from 100 cm^{-1} to 450 cm^{-1}, which is significantly more than those observed in TMDs with higher crystal symmetries[42]. These Raman peaks are mostly caused by the low crystal symmetry and are associated with fundamental Raman modes coupled to each other and to acoustic phonons. The most prominent Raman peaks are at 135, 200, 230 and 390 cm^{-1}. It has been pointed out that the relatively broad peaks of ReSSe might be due to lower quality of the alloy compared with the parent ReS_2 or $ReSe_2$ compounds. Figure 2b plots the peak positions of the main Raman peaks as a function of layer thickness. Interestingly, the peak positions of the Raman spectra are barely dependent on the layer thickness. Comparison between the Raman spectra of monolayer and bulk ReSSe only shows a slight difference. Such independency of the Raman peaks of ReSSe on the number of layers indicates that the lattice vibrations between adjacent layers in ReSSe are very weak, which might be attributed to the weak interlayered interaction energy[33], although one should note that the relationship between the interlayer binding energy and phonon modes is nontrivial.

Figure 3 shows theoretical band structures for monolayer ReS_2 and $ReSe_2$ along the high-symmetry lines determined by the in-plane reciprocal lattice vectors b_1 and b_2. The band structures were obtained using the local density approximation (LDA) and the Perdew-Burke-Ernzerhof (PBE) generalized gradient approximation of density functional theory (DFT). The structure of both materials is a distorted hexagonal lattice with a 12-atom unit cell, which was relaxed within DFT. In ReS_2, the in-plane lattice vectors are of length 6.28 Å and 6.38 Å and at an angle of 61.25 degrees according to the LDA (and of length 6.40 Å and 6.50 Å and at an angle of 61.16 degrees according to the PBE functional), while in $ReSe_2$, the in-plane lattice vectors are of length 6.51 Å and 6.64 Å and at an angle of 61.28 degrees according to the LDA (and of length 6.65 Å and 6.77 Å and at an angle of 61.21 degrees according to the PBE functional).

We find a semiconducting band structure and a decent qualitative agreement between the LDA and PBE results. The valence band is found to be very flat. Both functionals place the conduction-band minimum at the Γ point, but the valence-band maximum away from the Γ point. Semilocal DFT is known to underestimate band gaps and therefore the real quasiparticle band gap is expected to be larger than those predicted in Figure 3. In addition, semilocal DFT is not very reliable at calculating structural parameters in Peierls-distorted systems[43-45], which may be a further source of inaccuracy and could be the reason for the calculations predicting an indirect band gap; despite this, we find that the DFT-calculated structure displays a substantial Peierls distortion. In ReS_2 the length of the Re-Re bond ranges between 2.67 Å and 2.85 Å according to the LDA (and between 2.71 Å and 2.90 Å according to the PBE functional), while in $ReSe_2$ it ranges between 2.70 Å and 2.94 Å according to the LDA (and between 2.75 Å and 3.01 Å according to the PBE functional).

Comparing the band structures of monolayer ReS_2 and $ReSe_2$, we find that their valence band structures are very similar, and so are the edges of the conduction band structures. This suggests that the band gaps of ReSSe alloys can be approximated by a linear regression between the band gap of ReS_2 and $ReSe_2$. For this purpose we use the energy gap at the Γ point, since the valence band is flat around the band edge. Table 1 shows the comparison between the band gaps of ReS_2, $ReSe_2$, and the estimated band gap of ReSSe if the S/Se ratio is equal to 1. We report the energy gap at the Γ point, since the valence band is flat around the band edge. The DFT-PBE gap is in reasonable agreement with the measured gap of 1.3 eV despite the well-known underestimation of the band gap in DFT. This agreement is probably fortuitous, resulting

from the partial cancellation of the quasiparticle correction and the exciton binding in low-dimensional materials. Linear regression is not expected to be accurate for the exciton binding energy. We have studied randomly chosen configurations of the ReSSe alloy to test the validity of the linear interpolation of the gap. One of the configurations is illustrated in Figure 1a, where the Se atoms are highlighted in yellow. We have found that the band gap in the alloy agrees with the linear regression estimate within 0.01 eV, confirming that the use of a linear regression is justified. In conclusion, our DFT calculations strongly support the idea that it is possible to engineer the band gap of ReSSe by varying the S-Se ratio.

A field-effect transistor based on a ReSSe thin flake with a thickness of about 3 nm was fabricated and studied. The insets of Figure 4b show a typical optical image of the device and the height profile of the channel. The I_d - V_d and I_d - V_g curves of the device were measured and are shown in Figures 4a and b. the I_d - V_d data exhibit a slight superlinear behaviour at low drain bias, which suggests that the electrons are injected through a Schottky barrier at the metal-semiconductor interface. Figure 4b shows the transfer characteristic measured at three different drain biases, V_d =1 V, 3 V and 5 V, respectively. The device shows a typical n-type behaviour. The on/off ratio at V_d = 1 V is larger than 10^5, similar to the reported on/off ratios for MoS_2, WS_2, and WSe_2 devices, and is explained by the large band gaps. The mobility of the ReSSe device is deduced by fitting the linear range in the transfer curve from V_g = 20 V to V_g = 50 V. The mobility is calculated to be 3 $cm^2V^{-1}s^{-1}$, using the equation $\mu=dI_d/dV_g\times(L/WC_iV_d)$, where L is channel length, W is the channel width, C_i is the capacitance between the channel and the back gate per unit area ($C_i = \varepsilon_0 \varepsilon_r/d$, where ε_0 is the vacuum permittivity, ε_r is the relative permittivity, and d is the thickness of the SiO_2 layer). The mobility is comparable with compounds such as GaS and MoS_2[46]. It is well known that trap/impurity states exist at the SiO_2/Si surface in the bottom-gate transistor and the scattering from these charged impurities degrades the carrier mobility of the device. Removing surface traps/impurities in the bottom-gate dielectric is expected to improve the mobility of ReSSe-based transistors[47]. In addition, the conductivity shows clear dependence along different structure axes (not shown). We have measured the transfer characteristics along the in-plane crystal axes on a separate device made specifically for analysing the anisotropy in the mobility; the evaluated mobilities along the b-axis and a-axis are 2.6 $cm^2V^{-1}s^{-1}$ and 1.4 $cm^2V^{-1}s^{-1}$ respectively, giving a mobility difference ratio of 1.8(6). Due to the mobility being proportional to the inverse effective mass tensor, the ratio of the above mobilities can be corresponded to the ratio of effective masses at the conduction band minimum along the ΓX and ΓY directions. We find this ratio to be 1.9(3) from the DFT-PBE calculations when averaging over the four random configurations of ReSSe alloys considered, which matches the measured value quite well. Note that DFT-LDA predicts a larger ratio of 2.8(6).

To further study the transport properties of the ReSSe transistor, we performed temperature dependent measurements from room temperature down to 100 K. Figures 4c and 4d show the temperature dependent transfer and output curves. As the temperature decreases from room temperature, the drain voltage first increases slightly and then decreases gradually. The temperature dependence of the drain current and the mobility is shown in the inset of Figure 4c and 4d, respectively. The temperature dependence is characterized by a peak at 240 K. Below 240 K, we observe a decrease of the mobility as the temperature is lowered down to 100 K. This behaviour is consistent with the mobility being limited by scattering from charged impurities[48]. Increasing the temperature above 240 K also results in a strong decrease in the mobility from its peak value. This is related to electron-phonon scattering, which becomes the dominant scattering mechanism at higher temperatures.

The photoresponse properties of devices based on few-layer ReSSe were investigated by monitoring the photocurrent change under an applied drain voltage while tuning the incident light power and wavelength under vacuum condition. Figure 5a shows the photocurrent change as a function of the drain voltage with gate voltage of 0 V, under excitation by different intensities of light. Under excitation by light of wavelength 532 nm, the device can generate an obvious photocurrent even under illumination with an optical power of only 3 mW/cm^2. The photocurrent increases gradually as the driving drain voltage increases. Figure 5b shows the light-power dependence of the photocurrent, which can be expressed by a simple power law, on a log-log scale. The complex processes of electron-hole generation, trapping, and recombination within the semiconductor contribute to the nonlinear behaviour of the light-power dependence. One of the most important parameters for a photodetector is its photoresponsivity R, which is the ratio of the generated photocurrent to the incident optical power. Figure 5d shows the photoresponsivity R deduced from Figure 5b. At low illumination intensities, the device reaches a photoresponsivity of 8 A/W, at least an order of magnitude higher than both graphene photodetectors and the BP phototransistors that have recently been widely studied[49]. The high photoresponsivity makes ReSSe a promising material for applications in optoelectronic devices.

Broadband photoresponse is important for a photodetection device. Only if the photon energy of the incident light is greater than the band gap of the active material can the carriers be excited and generate the photocurrent under the applied drain voltage. As shown in Figure 5c, when the wavelength of the incident light is reduced, the photocurrent is enhanced, which is due to the higher absorption coefficient being higher at short wavelength than at long wavelength. The more light is absorbed by the channel, the more electron-hole pairs can be generated, which also contributes to the increase of the photocurrent produced by short-wavelength excitation. Because the gap of the ReSSe sample is around 1.39 eV, the

device can be used in a wide range, from near infrared to ultraviolet.

Schottky barriers have a large effect on photoresponse properties. It is well known that the gate voltage can modulate the Schottky barrier at the interface between the electrode and channel materials. So we investigated the gate-voltage modulation of photocurrent generation with the 532 nm laser illumination. The light power is fixed at around 100 mW/cm^2. Figure 6a shows the drain-voltage change as a function of gate voltage with and without illumination. By subtracting the dark current from the drain current generated under illumination, we can clearly see the gate modulation of the photocurrent (Figure 6b), which is attributed to the reduced Schottky barrier when a large, positive gate voltage is applied.

Conclusions

In conclusion, we have studied the electronic and photoresponsive properties of atomically thin ReSSe. We have made an n-type few-layered ReSSe transistor, and the electron mobility is found to be about 3 cm^{2}V^{-1}s^{-1}. Because of the direct-band-gap nature of ReSSe, photosensitive devices based on few-layer ReSSe exhibit a very high photoresponsivity, up to 8 A/W. In combination with large-area material preparation methods such as liquid scale exfoliation or chemical vapour deposition, the composition-dependent band gaps of ReSSe alloys make ReSSe a promising material for optoelectronic applications, and could enable the fabrication of low-cost and efficient optoelectronic devices.

METHODS

Sample preparation. ReSSe single crystal was grown by the chemical vapor transport method. Thin flakes of ReSSe were mechanically exfoliated on SiO_2/Si substrates and identified under microscope. The thickness of the ReSSe flakes was measured by atomic force microscopy (AFM, Cypher S). Raman measurements were performed in a Witec system in backscattering configuration. The excitation was provided by visible laser light (λ = 532 nm) through a 100× objective (NA = 0.95). To avoid laser-induced modification or ablation of samples, all spectra were recorded at low power levels. Optical absorption spectra were measured using a Jasco MSV-5200 microscopic spectrophotometer.

Fabrication of the field-effect transistor. First, ReSSe flakes were obtained by mechanical exfoliation of bulk single crystals on a Si substrate and identified by optical microscopy. The electrodes [Ti/Au (5/50 nm)] were then patterned using standard photolithography, electron-beam metal deposition, and lift-off.

Optoelectronic measurement. All the electronic and optoelectronic characterization was performed in a probe station under vacuum condition at room temperature, and recorded by an Agilent 1500A semiconductor analyser. The light excitation was provided by diode pumped solid state lasers operated in continuous wave mode with wavelengths of 405 nm, 532 nm, 633 nm, and 670 nm.

DFT calculations. We used the VASP[50] and CASTEP[51] density functional theory (DFT) codes to calculate the atomic and electronic structures of ReS_2, $ReSe_2$, and 4 random configurations of the ReSSe alloy. We used a plane-wave basis set with a cutoff energy of 680 eV, while the Brillouin zone was sampled by a 17×17 Monkhorst-Pack grid. A structural optimization was performed on the lattice until all the atomic forces were less than 5 meV/Å. We used an artificial periodicity of 15 Å in the out-of-plane direction.

Acknowledgement. This work is supported by the Singapore National Research Foundation under NRF RF Award No. NRF-RF2013-08, the start-up funding from Nanyang Technological University (M4081137.070). H.J.F. thanks the support from the Ministry of Education of Singapore (Grant No. MOE2011-T3-1-005).

Notes and references

1. Pospischil, A.; Humer, M.; Furchi, M. M.; Bachmann, D.; Guider, R.; Fromherz, T.; Mueller, T. CMOS-compatible graphene photodetector covering all optical communication bands. *Nature Photonics* 2013, 7, 892-896.
2. Novoselov, K. S.; Geim, A. K.; Morozov, S.; Jiang, D.; Zhang, Y.; Dubonos, S. a.; Grigorieva, I.; Firsov, A. Electric field effect in atomically thin carbon films. *Science* 2004, 306, 666-669.
3. Mueller, T.; Xia, F.; Avouris, P. Graphene photodetectors for high-speed optical communications. *Nature Photonics* 2010, 4, 297-301.
4. Schwierz, F. Graphene transistors. *Nature Nanotechnology* 2010, 5, 487-496.
5. Roy, K.; Padmanabhan, M.; Goswami, S.; Sai, T. P.; Ramalingam, G.; Raghavan, S.; Ghosh, A. Graphene-MoS_2 hybrid structures for multifunctional photoresponsive memory devices. *Nature Nanotechnology* 2013, 8, 826-830.
6. Novoselov, K. S.; Fal, V.; Colombo, L.; Gellert, P.; Schwab, M.; Kim, K. A roadmap for graphene. *Nature* 2012, 490, 192-200.
7. Novoselov, K.; Jiang, D.; Schedin, F.; Booth, T.; Khotkevich, V.; Morozov, S.; Geim, A. Two-dimensional atomic crystals. *Proc. Natl. Acad. Sci. USA* 2005, 102, 10451-10453.
8. Mak, K. F.; McGill, K. L.; Park, J.; McEuen, P. L. The valley Hall effect in MoS_2 transistors. *Science* 2014, 344, 1489-1492.
9. Zeng, H.; Dai, J.; Yao, W.; Xiao, D.; Cui, X. Valley polarization in MoS_2 monolayers by optical pumping. *Nature nanotechnology* 2012, 7, 490-493.
10. Yu, W. J.; Li, Z.; Zhou, H.; Chen, Y.; Wang, Y.; Huang, Y.; Duan, X. Vertically stacked multi-heterostructures of layered materials for logic transistors and complementary inverters. *Nature materials* 2013, 12, 246-252.
11. Du, X.; Skachko, I.; Barker, A.; Andrei, E. Y. Approaching ballistic transport in suspended graphene. *Nature Nanotechnology* 2008, 3, 491-495.
12. Dean, C.; Young, A.; Meric, I.; Lee, C.; Wang, L.; Sorgenfrei, S.; Watanabe, K.; Taniguchi, T.; Kim, P.; Shepard, K. Boron nitride substrates for high-quality graphene electronics. *Nature Nanotechnology* 2010, 5, 722-726.
13. Lee, C.; Wei, X.; Kysar, J. W.; Hone, J. Measurement of the elastic properties and intrinsic strength of monolayer graphene. *science* 2008, 321, 385-388.

14. Balandin, A. A.; Ghosh, S.; Bao, W.; Calizo, I.; Teweldebrhan, D.; Miao, F.; Lau, C. N. Superior thermal conductivity of single-layer graphene. *Nano Lett* 2008, 8, 902-907.
15. Georgiou, T.; Jalil, R.; Belle, B. D.; Britnell, L.; Gorbachev, R. V.; Morozov, S. V.; Kim, Y.-J.; Gholinia, A.; Haigh, S. J.; Makarovsky, O. Vertical field-effect transistor based on graphene-WS_2 heterostructures for flexible and transparent electronics. *Nature nanotechnology* 2013, 8, 100-103.
16. Gong, Y.; Lin, J.; Wang, X.; Shi, G.; Lei, S.; Lin, Z.; Zou, X.; Ye, G.; Vajtai, R.; Yakobson, B. I. Vertical and in-plane heterostructures from WS_2/MoS_2 monolayers. *Nature materials* 2014, **13**, 1135–1142.
17. Yoon, Y.; Ganapathi, K.; Salahuddin, S. How good can monolayer MoS_2 transistors be? *Nano letters* 2011, 11, 3768-3773.
18. Hong, X.; Kim, J.; Shi, S.-F.; Zhang, Y.; Jin, C.; Sun, Y.; Tongay, S.; Wu, J.; Zhang, Y.; Wang, F. Ultrafast charge transfer in atomically thin MoS_2/WS_2 heterostructures. *Nature nanotechnology* 2014, **9**, 682–686.

19. Mak, K. F.; Lee, C.; Hone, J.; Shan, J.; Heinz, T. F. Atomically thin MoS_2: a new direct-gap semiconductor. *Physical Review Letters* 2010, 105, 136805.
20. Rodin, A.; Carvalho, A.; Neto, A. C. Strain-induced gap modification in black phosphorus. *Physical review letters* 2014, 112, 176801.
21. Tran, V.; Soklaski, R.; Liang, Y.; Yang, L. Layer-controlled band gap and anisotropic excitons in few-layer black phosphorus. *Physical Review B* 2014, 89, 235319.
22. Liu, H.; Neal, A. T.; Zhu, Z.; Luo, Z.; Xu, X.; Tománek, D.; Ye, P. D. Phosphorene: an unexplored 2D semiconductor with a high hole mobility. *ACS nano* 2014, 8, 4033-4041.
23. Li, L.; Yu, Y.; Ye, G. J.; Ge, Q.; Ou, X.; Wu, H.; Feng, D.; Chen, X. H.; Zhang, Y. Black phosphorus field-effect transistors. *Nature nanotechnology* 2014, 9, 372-377.
24. Youngblood, N.; Chen, C.; Koester, S. J.; Li, M. Waveguide-integrated black phosphorus photodetector with high responsivity and low dark current. *Nature Photonics* 2015, **9**, 247–252.
25. Buscema, M.; Groenendijk, D. J.; Steele, G. A.; van der Zant, H. S.; Castellanos-Gomez, A. Photovoltaic effect in few-layer black phosphorus PN junctions defined by local electrostatic gating. *Nature communications* 2014, 5, 4561.
26. Wang, X.; Jones, A. M.; Seyler, K. L.; Tran, V.; Jia, Y.; Zhao, H.; Wang, H.; Yang, L.; Xu, X.; Xia, F. Highly anisotropic and robust excitons in monolayer black phosphorus. *Nature nanotechnology* 2015, 10, 517–521.
27. Xia, F.; Wang, H.; Jia, Y. Rediscovering black phosphorus as an anisotropic layered material for optoelectronics and electronics. *Nature communications* 2014, 5, 4458.
28. Qiao, J.; Kong, X.; Hu, Z.-X.; Yang, F.; Ji, W. High-mobility transport anisotropy and linear dichroism in few-layer black phosphorus. *Nature communications* 2014, 5, 4475.
29. Island, J. O.; Steele, G. A.; van der Zant, H. S.; Castellanos-Gomez, A. Environmental instability of few-layer black phosphorus. *2D Materials* 2015, 2, 011002.
30. Murray, H.; Kelty, S.; Chianelli, R.; Day, C. Structure of rhenium disulfide. *Inorg Chem* 1994, 33, 4418-4420.
31. Wolverson, D.; Crampin, S.; Kazemi, A. S.; Ilie, A.; Bending, S. J. Raman spectra of monolayer, few-layer, and bulk $ReSe_2$: An anisotropic layered semiconductor. *ACS nano* 2014, 8, 11154-11164.
32. Liu, E.; Fu, Y.; Wang, Y.; Feng, Y.; Liu, H.; Wan, X.; Zhou, W.; Wang, B.; Shao, L.; Ho, C.-H. Integrated digital inverters based on two-dimensional anisotropic ReS_2 field-effect transistors. *Nature communications* 2015, 6.
33. Tongay, S.; Sahin, H.; Ko, C.; Luce, A.; Fan, W.; Liu, K.; Zhou, J.; Huang, Y.-S.; Ho, C.-H.; Yan, J. Monolayer behaviour in bulk ReS2 due to electronic and vibrational decoupling. *Nature communications* 2014, 5, 3252.
34. Feng, J.; Qian, X.; Huang, C.-W.; Li, J. Strain-engineered artificial atom as a broad-spectrum solar energy funnel. *Nature Photonics* 2012, 6, 866-872.
35. Hui, Y. Y.; Liu, X.; Jie, W.; Chan, N. Y.; Hao, J.; Hsu, Y.-T.; Li, L.-J.; Guo, W.; Lau, S. P. Exceptional tunability of band energy in a compressively strained trilayer MoS2 sheet. *Acs Nano* 2013, 7, 7126-7131.
36. Ghorbani-Asl, M.; Borini, S.; Kuc, A.; Heine, T. Strain-dependent modulation of conductivity in single-layer transition-metal dichalcogenides. *Physical Review B* 2013, 87, 235434.
37. Komsa, H.-P.; Krasheninnikov, A. V. Electronic structures and optical properties of realistic transition metal dichalcogenide heterostructures from first principles. *Physical Review B* 2013, 88, 085318.
38. Kutana, A.; Penev, E. S.; Yakobson, B. I. Engineering electronic properties of layered transition-metal dichalcogenide compounds through alloying. *Nanoscale* 2014, 6, 5820-5825.
39. Li, H.; Duan, X.; Wu, X.; Zhuang, X.; Zhou, H.; Zhang, Q.; Zhu, X.; Hu, W.; Ren, P.; Guo, P. Growth of Alloy MoS2 x Se2 (1–x) Nanosheets with Fully Tunable Chemical Compositions and Optical Properties. *J Am Chem Soc* 2014, 136, 3756-3759.
40. Chen, Y.; Xi, J.; Dumcenco, D. O.; Liu, Z.; Suenaga, K.; Wang, D.; Shuai, Z.; Huang, Y.-S.; Xie, L. Tunable band gap photoluminescence from atomically thin transition-metal dichalcogenide alloys. *Acs Nano* 2013, 7, 4610-4616.
41. Wang, G.; Robert, C.; Suslu, A.; Chen, B.; Yang, S.; Alamdari, S.; Gerber, I. C.; Amand, T.; Marie, X.; Tongay, S. Spin-orbit engineering in transition metal dichalcogenide alloy monolayers. *arXiv preprint arXiv:1506.08114* 2015.
42. Li, H.; Zhang, Q.; Yap, C. C. R.; Tay, B. K.; Edwin, T. H. T.; Olivier, A.; Baillargeat, D. From bulk to monolayer MoS_2: evolution of Raman scattering. *Adv Funct Mater* 2012, 22, 1385-1390.
43. Mintmire, J.; White, C. Local-density-functional results for the dimerization of trans-polyacetylene: Relationship to the band-gap problem. *Physical Review B* 1987, 35, 4180.
44. Rusznyak, A.; Zólyomi, V.; Kürti, J.; Yang, S.; Kertesz, M. Bond-length alternation and charge transfer in a linear carbon chain encapsulated within a single-walled carbon nanotube. *Physical Review B* 2005, 72, 155420.
45. Al-Backri, A.; Zólyomi, V.; Lambert, C. J. Electronic properties of linear carbon chains: Resolving the controversy. *The Journal of chemical physics* 2014, 140, 104306.
46. Hu, P.; Wang, L.; Yoon, M.; Zhang, J.; Feng, W.; Wang, X.; Wen, Z.; Idrobo, J. C.; Miyamoto, Y.; Geohegan, D. B. Highly responsive ultrathin GaS nanosheet photodetectors on rigid and flexible substrates. *Nano Lett.* 2013, 13, 1649-1654.
47. Chamlagain, B.; Li, Q.; Ghimire, N. J.; Chuang, H.-J.; Perera, M. M.; Tu, H.; Xu, Y.; Pan, M.; Xaio, D.; Yan, J. Mobility Improvement and Temperature Dependence in $MoSe_2$ Field-Effect Transistors on Parylene-C Substrate. *ACS nano* 2014, 8, 5079-5088.
48. Radisavljevic, B.; Kis, A. Mobility engineering and a metal–insulator transition in monolayer MoS_2. *Nature materials* 2013, 12, 815-820.
49. Buscema, M.; Groenendijk, D. J.; Blanter, S. I.; Steele, G. A.; van der Zant, H. S.; Castellanos-Gomez, A. Fast and broadband

photoresponse of few-layer black phosphorus field-effect transistors. *Nano Lett.* 2014, 14, 3347-3352.
50. Kresse, G.; Furthmüller, J. Efficient iterative schemes for ab initio total-energy calculations using a plane-wave basis set. *Physical Review B* 1996, 54, 11169.
51. Clark, S. J.; Segall, M. D.; Pickard, C. J.; Hasnip, P. J.; Probert, M. I.; Refson, K.; Payne, M. C. First principles methods using CASTEP. *Z Kristallogr* 2005, 220, 567-570.

Journal Name

COMMUNICATION

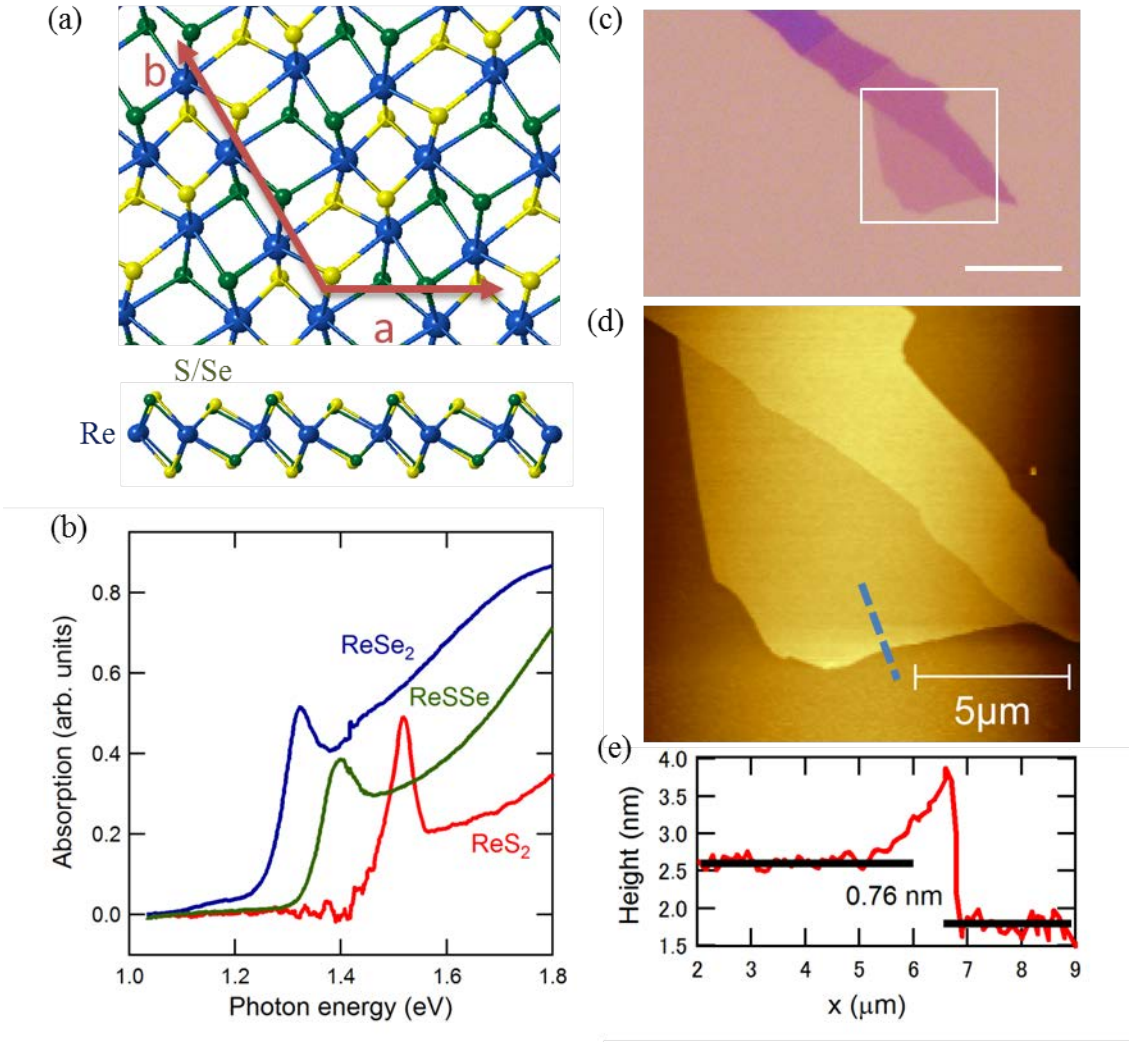

Figure 1. (a) Crystal structure of the ReX_2 compound. (b) Absorption spectrum of the ReS_2, ReSSe, and $ReSe_2$. (c) Typical optical image of a ReSSe flake with regions of different thickness. Scale bar: 10 μm. (d) AFM image of the flake shown in panel (c). (e) The height profile along the dashed line in (d) shows monolayer thickness.

Journal Name

COMMUNICATION

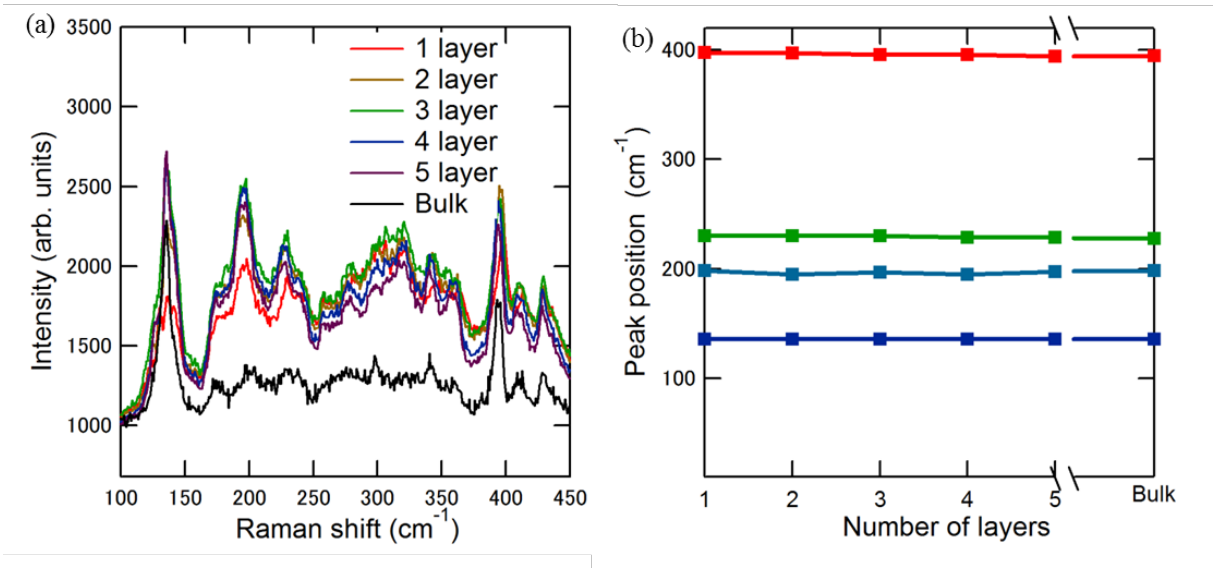

Figure 2. (a) Raman spectra of ReSSe flakes with thicknesses ranging from monolayer to five layers, and bulk ReSSe. Four clear main peaks are observed. (b) Positions of the main peaks as a function of the number of layers. The peak positions are barely dependent on the thickness of the flake, indicating weak inter-layer interactions.

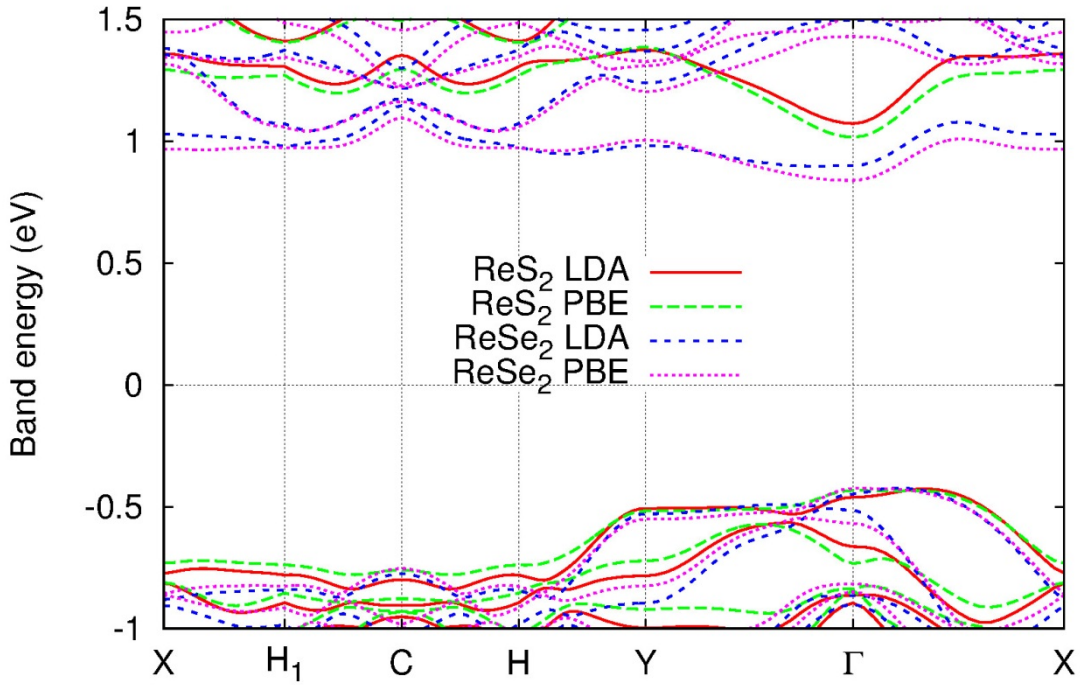

Figure 3. DFT band structures of ReS_2 and $ReSe_2$, calculated using the local density approximation and the PBE generalized gradient approximation along high symmetry lines in the two-dimensional reciprocal space of the monolayer.

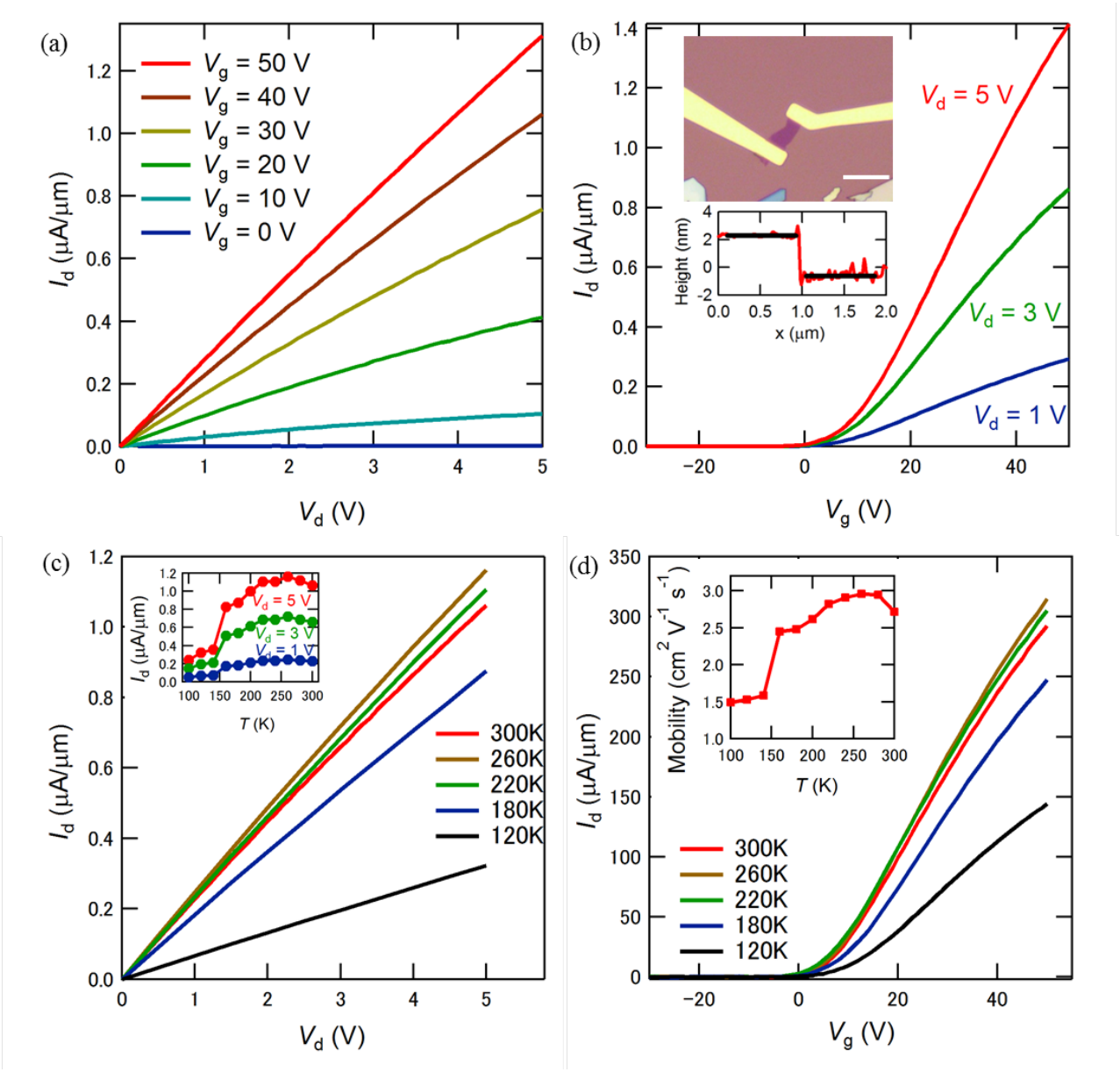

Figure 4. (a) I_d-V_d curve of a ReSSe thin-flake transistor with a thickness of about 3 nm. The near-linear I_d-V_d dependence at low drain voltage indicates a small Schottky barrier between the metal contact and the channel. (b) I_d-V_g curve of the ReSSe transistor with a drain voltage of 1 V, 3 V, and 5 V. The device shows n-type behaviour. The insets show an optical image of the device and the height profile for the channel. Scale bar: 10 μm. (c) I_d-V_d curve and (d) I_d-V_g curve at different temperatures. The drain voltage first increases when the temperature decreases from 300 K, and then decreases when the temperature falls below 240 K. The inset of panel (c) shows the drain-current change as a function of temperature at a gate voltage of 30 V. The inset of panel (d) shows the temperature dependence of the mobility deduced from the I_d-V_g curve.

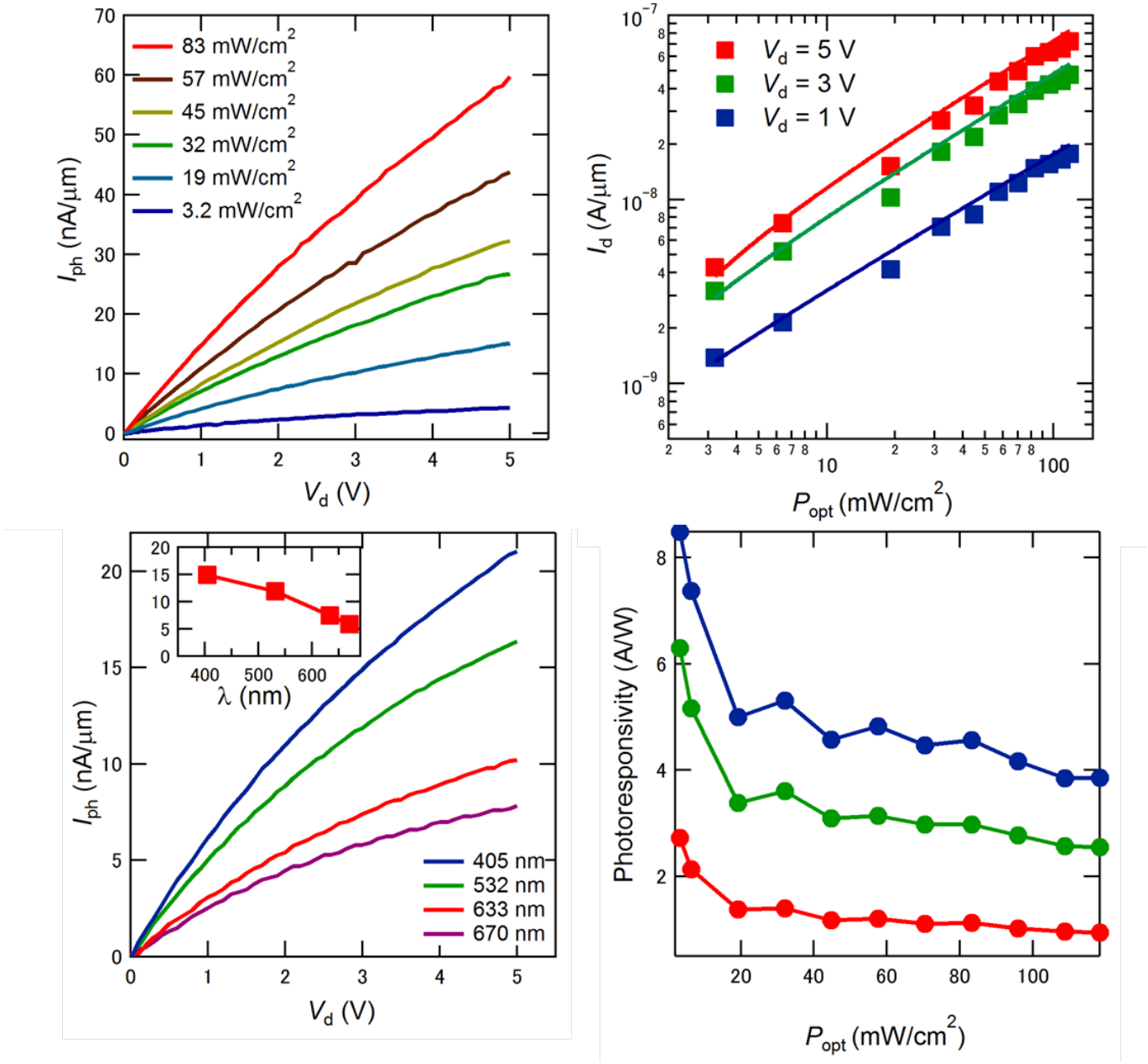

Figure 5. (a) Photocurrent as a function of drain voltage under different light intensities. (b) Photocurrent as a function of intensity on a log-log scale, with drain voltages of 1 V, 3 V, and 5 V. The solid lines are the power-law fits with an exponent of 0.73. (c) Photocurrent as a function of drain voltage at different excitation wavelengths. The inset shows the photocurrent at a drain voltage of 4 V as a function of excitation wavelength. (d) Photoresponsivity as a function of the light intensity as deduced from panel (b).

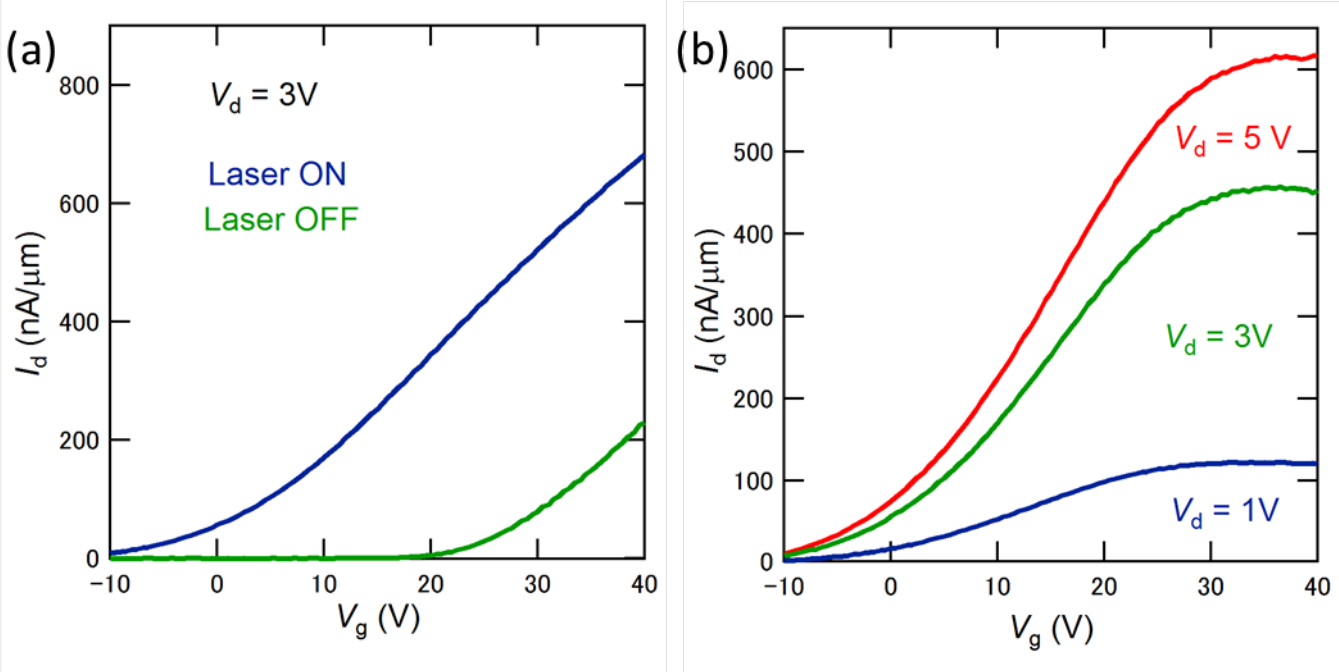

Figure 6. (a) I_d-V_d curve of the ReSSe field-effect transistor, with and without illumination. (b) Photocurrent as a function of gate voltage. The photocurrent is deduced by taking the difference of the drain currents with and without illumination. The photocurrent can be strongly modulated by the gate voltage.

Table 1: DFT direct (Γ_c-Γ_v) band gaps in ReS_2, $ReSe_2$, and ReSSe. In the case of ReSSe we use values averaged over four randomly chosen configurations, one of which is illustrated in Figure 1a (the yellow highlighted chalcogen atoms are Se, the non-highlighted ones S atoms). The last column shows the linear regression estimate of the ReSSe band gap, which is in very good agreement with the actual average gap of the randomly chosen ReSSe alloys.

	ReS_2	$ReSe_2$	ReSSe	Est. ReSSe
LDA band gap	1.533 eV	1.348 eV	1.44(3) eV	1.441 eV
PBE band gap	1.448 eV	1.262 eV	1.36(3) eV	1.355 eV